Structure and dynamics correlations of photoinduced charge separation in rigid conjugated linear donor–acceptor dyads towards photovoltaic applications

Jianchang Guo,[ab] Yongye Liang,[a] Shengqian Xiao,[a] Jodi M. Szarko,[d] Michael Sprung,[c] Mrinmay K. Mukhopadhyay,[c] Jin Wang,[c] Luping Yu*[a] and Lin X. Chen*[bd]

Received (in Gainesville, FL, USA) 9th December 2008, Accepted 4th February 2009
First published as an Advance Article on the web 19th March 2009
DOI: 10.1039/b821941a

The rates of photoinduced charge separation (CS) and charge recombination (CR) of four rigidly linked donor (D)–acceptor (A) dyads that were synthesized as intramolecular p/n junctions were obtained by optical transient absorption spectroscopy in solutions and self-assembled films. The CS processes were much more efficient than CR processes for all dyads in both solutions and films, which is preferable for photovoltaic applications. The rates of CR processes in covalently linked dyad films were slower than those in non-covalently linked D (*i.e.* oligothiophene (OTH)) and A (*i.e.* perylenediimide (PDI)) mixtures, demonstrating that the covalent linker may have reduced the probability of geminate recombination of charges due to direct face-to-face packing between D and A. Although both the CS and CR rates of the four dyads were similar with respect to one another in solution, they differed from one another in films, with the slowest CR rate observed in the dyad connected to a bulky alkyl group that hindered packing. After annealing, the CR rates of all films increased non-uniformly, and the extent of increase was correlated to structural changes as evidenced by the grazing-incident X-ray scattering (GIXS).

Introduction

Organic semiconducting materials are an attractive alternative to silicon in solar cells because they exhibit encouraging characteristics such as easier processing, lower cost, and greater flexibility.[1–4] Most current organic photovoltaic (OPV) cells use bulk heterojunction (BHJ) composite materials such as conducting polymer/C_{60},[5] polymer/polymer mixtures,[6] and polymer/inorganic hybrid nanomaterials.[7–9] However, the highest OPV power conversion efficiency (PCE) is currently ~5.5%,[5,10,11] which is much lower than the efficiency necessary for widespread viability. To achieve a higher PCE, a photovoltaic material must be efficient in light harvesting, charge carrier generation, and electron/hole transport. It must also interface well with the electrodes for charge collection.[3] A fundamental understanding of energy and charge carrier generation/flow at the molecular level, and their correlation to molecular structures, is crucial for rational exploration of new materials for OPV applications.

One of the main obstacles to achieving high efficiency in the current BHJ solar cells is low exciton dissociation efficiency, which is due to shorter exciton diffusion lengths (~5–10 nm) than D and A domain dimensions.[12,13] When the D and A domain dimensions are larger than the exciton diffusion length, a significant fraction of photon-generated excitons decay to the ground state before they can diffuse to a domain boundary and undergo charge separation.[14–16] This problem has been observed in spin-coated, π-conjugated polymer/C_{60} composites.[17,18] To remedy this problem, "molecular p–n junctions" are constructed by covalently linking the conjugated D and A blocks, which transforms the exciton dissociation from an inefficient inter-domain process into an efficient intra-molecular charge separation process. Several examples of covalently linked oligomers (as D) and fullerenes (as A)[19–27] as well as pentaphenylenes and perylenediimide based multi-chromophore D–A arrays[28–30] have been reported in the literature. We have previously demonstrated in a covalently linked, π-conjugated D–A quartet molecule that the CS rate (k_{CS}) can be several orders of magnitude faster than the CR rate (k_{CR}) in solutions[31] and films with different D and A arrangements, such as a non-covalent random mixture, a covalently linked quartet monomer, and its polymer.[32] These studies suggest that the covalent linkage between D and A blocks and the extension of π-conjugation facilitate charge carrier transport away from D–A interfaces, resulting in a relatively long-lived CS state with potential benefits to OPV operation. The challenge for this type of molecular dyad in OPV applications is the charge carrier diffusion away from where they are separated to minimize the germination recombination, which will be achieved by self-assembled dual π-stacked D and A continuous channels resulting from the planar π-conjugated blocks investigated

[a] *Department of Chemistry, The University of Chicago, Chicago, Illinois 60637, USA. E-mail: lupinyu@uchicago.edu*
[b] *Chemical Sciences and Engineering Division, Argonne National Laboratory, Argonne, Illinois 60439, USA. E-mail: lchen@anl.gov*
[c] *X-ray Science Division, Advanced Photon Source, Argonne National Laboratory, Argonne, Illinois 60439*
[d] *Department of Chemistry, Northwestern University, Evanston, Illinois 60208, USA*

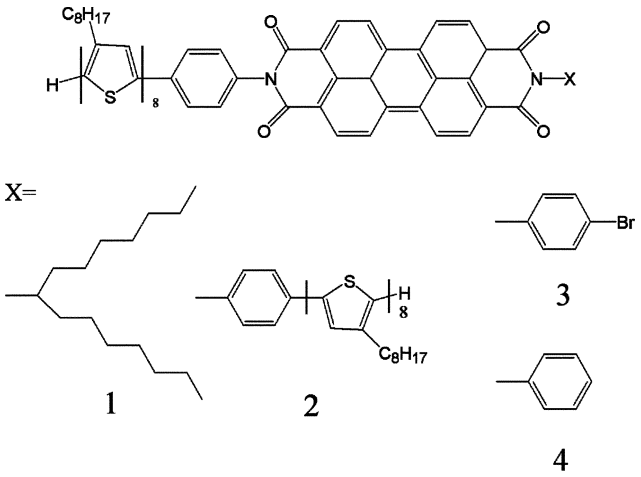

Fig. 1 Molecular structure of linear donor–acceptor block molecules labeled as **1**, **2**, **3** and **4**.

here. Such design will be verified by structural characterizations using X-ray diffraction and correlated with device efficiency studies in the future.

To guide synthetic efforts in diblock co-oligomers and copolymers, we investigated photoinduced CS and CR dynamics in a series of linearly connected oligothiophene–perylenediimide (**OTH–PDI**) diblock arrays with a rigid benzene linker. In this case, **OTH** and **PDI** are the D and A blocks, respectively (Fig. 1). While a quartet D–A molecule linked with flexible linkers from our previous study[31] permits several different conformations, the rigidly linked diblock systems presented here have better defined D–A orientations and distances. The end group attached to the terminal N atom of the **PDI** block was varied in order to tune electronic and geometric factors that may alter the molecular packing in films, or affect the lifetime of CS state and charge carrier transport. The k_{CS} and k_{CR} of these D–A arrays have been correlated to structural changes from solutions to films, especially those films after annealing. Our goal is to establish the correlation between photoinduced charge separation/recombination dynamics and molecular structures, which will guide new material discovery for OPV applications. The study presented here is the first step in correlating OPV properties with molecular structures, while our ultimate goal is to use the knowledge obtained here to rationally construct new OPV materials with desirable hierarchic structures from molecules to devices.

Experimental

Femtosecond transient absorption spectroscopy

Ultrafast transient absorption (TA) spectra and kinetics were carried out by a home-built Ti:sapphire laser system with an optical parametric amplifier (OPA) as described previously.[31] Excitation laser pulses were derived from either the second harmonic of the Ti:sapphire regenerative amplifier at 403–410 nm or the output of the OPA at 522–530 nm. White light continuum probe pulses were generated by focusing a few microjoules of the Ti:sapphire amplifier output onto a sapphire disk. The resulting probe beam was split to produce reference and measuring beams. The white light probe beam and the 300 nJ (~100 nJ with OPA output) pump beam were focused to a 0.3 mm diameter spot at the sample with a nearly collinear geometry. The optical density of the sample was kept below 0.4 at 410 nm, and the sample cuvette was 2 mm thick. The pump and probe pulses were about 90 fs at fwhm (full width at half-maximum), and the instrumental response function was 180 fs at fwhm.

Stock solutions of the linear donor–acceptor dyads and reference molecules were freshly made, and their integrity was monitored by UV-Vis spectroscopy during laser experiments. The solutions were purged with nitrogen gas through the sample cuvette sealed by a septum during the experiments. The films were spin-coated from a toluene solution at 2000 rpm. All measurements were carried out at room temperature.

Steady-state absorption and fluorescence spectra

UV-Vis absorption spectra were obtained using a Shimadzu UV-2401PC or UV-1609 spectrophotometer. The fluorescence spectra were taken by a PTI Fluorescence Master Series fluorometer or a Shimadzu RF-5301PC spectrofluorophotometer.

Electrochemistry

Cyclic voltammetry (CV) was performed on a CV-50W Voltammetric Analyzer (Bioanalytical Systems Inc.) in a conventional four-compartment cell in a solution of methylene chloride (0.1 M Bu_4NPF_6 as supporting electrolyte) at a scan rate of 100 mV s^{-1}. A Pt wire was used as the working electrode, another Pt wire was used as the counter electrode, and a Ag/AgCl electrode was used as the reference electrode. All oxidation and reduction potential values were calibrated against the oxidation of ferrocene.

Grazing incidence X-ray scattering (GIXS) measurements

Grazing-incidence small-angle X-ray scattering (GISAXS) and wide-angle X-ray scattering (GIWAXS) measurements were performed using beamline 8ID of the Advanced Photon Source (APS) at Argonne National Laboratory. Scattering intensities are expressed as a function of the scattering vector, $q = (4\pi/\lambda)\sin\theta$, where θ is the half scattering angle and $\lambda = 1.6868$ Å is the wavelength of the incident radiation. The d-spacing of a peak is $2\pi/q$.

The samples were kept under vacuum during irradiation to minimize the radiation damage of the films from the X-ray beam. A two-dimensional area MAR detector was used to collect the scattering image and was situated at 1942 and 280.9 mm from the sample for GISAXS and GIWAXS measurements, respectively. The photon energy of the X-ray beam was 7.35 keV. The films were illuminated at an incidence angle of about 0.2° so that the X-ray beam could penetrate the entire thickness of the film and only a small portion of the glass substrate, minimizing the background scattering from the substrate.

Results

UV-Vis absorption and emission spectra in solution

Fig. 2 shows UV-Vis spectra of **1–4** and the reference compounds, **PDI** and **OTH**, in toluene. The spectra obtained

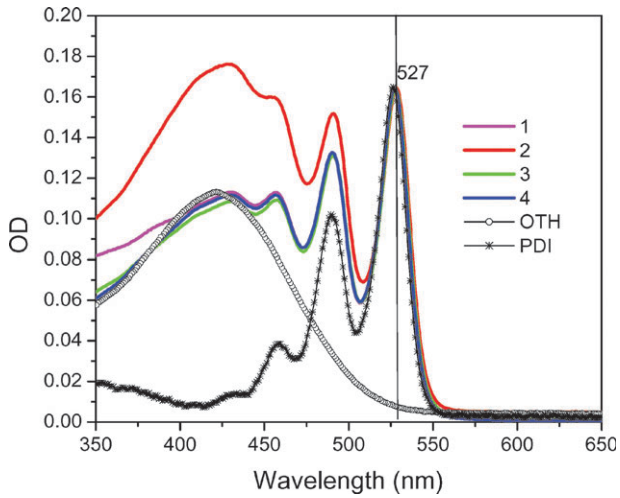

Fig. 2 UV-Vis spectra of the linear D–A dyads in toluene normalized at the peak absorption at 527 nm.

in THF (not shown) are similar but exhibit a 5 nm shift due to the increased polarity of the solvent. The broad peak around 422 nm for the molecules in toluene corresponds to the π–π* transition of the **OTH** block, and the sharp peak features at 527, 490, 460 nm are characteristic (0,0), (0,1) and (0,2) vibronic bands of the **PDI** block, respectively.[31] The spectra of **1–4** can be approximated by the superposition of **OTH** and **PDI** constituents, suggesting no strong interactions between the D and A blocks in the ground state. Intensity ratios of the (0,0) and (0,1) vibronic bands from the **PDI** block in **1–4** are approximately 1.6, similar to that of **PDI** alone in solution, and therefore there is no indication of aggregate formation.[33] The emission spectra of **1–4** obtained with 485 nm excitation exhibit two characteristic peaks at 535 and 578 nm due to the **PDI** emission (not shown). The fluorescence quantum yields in **1–4** with respect to the **OTH** emission were reduced by a factor of >100, providing evidence for charge transfer from the **OTH** block to the **PDI** block.

Electrochemical properties in solution

The electrochemical properties of **1–4** and reference molecules **OTH** and **PDI** were investigated by cyclic voltammetry (CV) in methylene chloride with 0.1 M *n*-$Bu_4N^+PF_6^-$. The CV curves of **1–4** exhibit three one-electron oxidation waves from the **OTH** moiety and two one-electron reduction waves from the **PDI** moiety (Table 1).

Photoinduced CS and CR dynamics in solution

The (0,0) transition energies obtained from fluorescence measurements for **OTH** and **PDI** blocks are 2.33 and 2.30 eV, respectively, both of which are significantly higher than the energy of **OTH**$^+$–**PDI**$^-$ at 1.30 eV (Fig. 3). Hence, the electron transfer *via* both $^1D^*$–A → D^+–A^- and D–$^1A^*$ → D^+–A^- can take place. Meanwhile, the emission spectra of the dyads resemble that of A* (not shown). Therefore the excitation of **OTH** unit at 403 nm will result in parallel pathways:[31] (1) energy transfer, $^1D^*$–A → D–$^1A^*$, and (2) electron transfer, $^1D^*$–A → D^+–A^-.

The CS and CR dynamics of **1–4** were measured by optical transient absorption (TA) spectroscopy with excitation wavelengths of 403 or 527 nm to preferentially excite **OTH** or **PDI**, respectively. TA spectra of **1** (Fig. 4) also represent similar TA spectra of **2–4** under the 403 nm excitation in toluene. The two negative ground state bleaching (GB) features at 490 and 530 nm of the **PDI** block reach their negative maxima at 1 ps delay, followed by a continuous recovery thereafter. The weak stimulated emission (SE) signal of **PDI*** at 578 nm appears at 0.2 ps. The broad excited state absorption (EA) of **PDI*** centered near 690 nm appears within 0.2 ps and subsequently evolves into a sharp peak at 715 nm within 2 ps. Similarly, this peak is also observed for **1** in THF at 710 nm within 0.5 ps after excitation (Fig. 4(b)). This sharp peak is indicative of the formation of **PDI**$^-$ due to the intramolecular charge separation,[31,34–36] and has been observed in the spectra of **PDI**$^-$ radicals generated electrochemically[37] and chemically.[36]

The differences between the sharp, strong absorption peak of **PDI**$^-$ at 710 nm and the broad, featureless absorption of ^{1}**PDI*** centered near 690 nm in solution have been characterized in our previous study,[31] as well as by others in literature.[26,34,35] The initial TA growth and decay in the region of 550 to 750 nm are due to a superimposed absorption from three sources, ^{1}**OTH***, ^{1}**PDI*** and **PDI**$^-$, generated through the CS process. The absorption of the anion **PDI**$^-$ in those linear D–A dyads is the dominate species because the excited states ^{1}**OTH*** and ^{1}**PDI*** are rapidly depleted due to the CS process. This claim is supported by the $>99\%$ quenched fluorescence spectra for these dyads. A small dip at 571–578 nm in the TA spectra within 200 fs after the excitation is due to the stimulated emission from a very small fraction of ^{1}**PDI*** formed *via* the direct excitation of **PDI** by 403 nm light or the energy transfer (Fig. 3). Because the absorption coefficient of **PDI** is much lower than that of **OTH** at 403 nm, the latter pathway is dominating. Therefore, the rise of the spectral feature of **PDI**$^-$ near 710 nm, although it is convoluted with **OTH*** and **PDI*** in the same spectral region, can be used to monitor the lower limit of the CS rates.

Based on the above analysis, the rise and decay of the peak near 710 nm are attributed to the absorption of **PDI**$^-$. These signals are used to monitor the CS and CR dynamics in **1–4**. Furthermore, both the appearance of **PDI**$^-$ and concurrent disappearance of the negative SE feature at 578 nm strongly suggest that CS occurs within 1–2 ps in toluene and <0.5 ps in THF. Hereafter, all the CS and CR dynamics of the dyads in the solution are monitored through the evolution of the **PDI**$^-$ anion peak at 715 nm (toluene) or 710 nm (THF).

The dynamics at 710 nm for **1** in THF has a bi-exponential rise with time constants of 180 fs and ~2 ps, as well as bi-exponential decay time constants of 14 ps and 63 ps. The average decay time constant can be evaluated according to $\tau_{avg} = A_1\tau_1 + A_2\tau_2$, where τ is the time constant and A is the percentage of the corresponding time component. The decay time constant is $\tau_{av} = 27$ ps in THF, which is ~17 times shorter than that in toluene. The time constants for CS and CR processes for **1–4** are listed in Table 2. The CS and CR kinetic traces for **1–4** in toluene with 403 nm excitation are similar, showing very little effect of the end groups on the CS and CR kinetics (Fig. 5).

Table 1 Half-wave potentials (*vs.* Fc/Fc^+) in methylene chloride (with 0.1 M n-$Bu_4N^+PF_6^-$) at room temperature (CV scan rate, 100 mV s^{-1})

	Oxidation potentials/V				Reduction potentials/V	
	PDI	**OTH**			**PDI**	
	$E_{ox(1)}$	$E_{ox(1)}$	$E_{ox(2)}$	$E_{ox(3)}$	$E_{red(1)}$	$E_{red(2)}$
1		0.22	0.36	0.74	−1.08	−1.3
2		0.20	0.35	0.69	−1.06	−1.22
3		0.30	0.42		−0.98	−1.17
4		0.17	0.32	0.65	−1.08	−1.25
OTH		0.22	0.66	1.05		
PDI	1.20				−1.16	−1.36

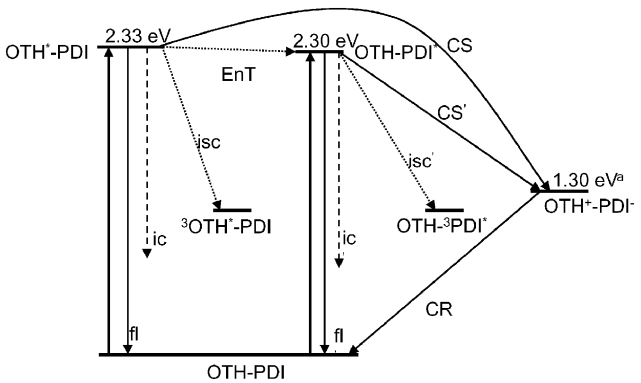

Fig. 3 Schematic energy diagram for photophysical processes in **1–4**, where CS represents charge separation; CR, charge recombination; EnT, energy transfer; isc, intersystem crossing; ic, internal conversion; and fl, fluorescence. [a]The energy for OTH^+–PDI^- is calculated as $E_{ox(1)} - E_{red(1)}$ (see Table 1) using **1** as an example.

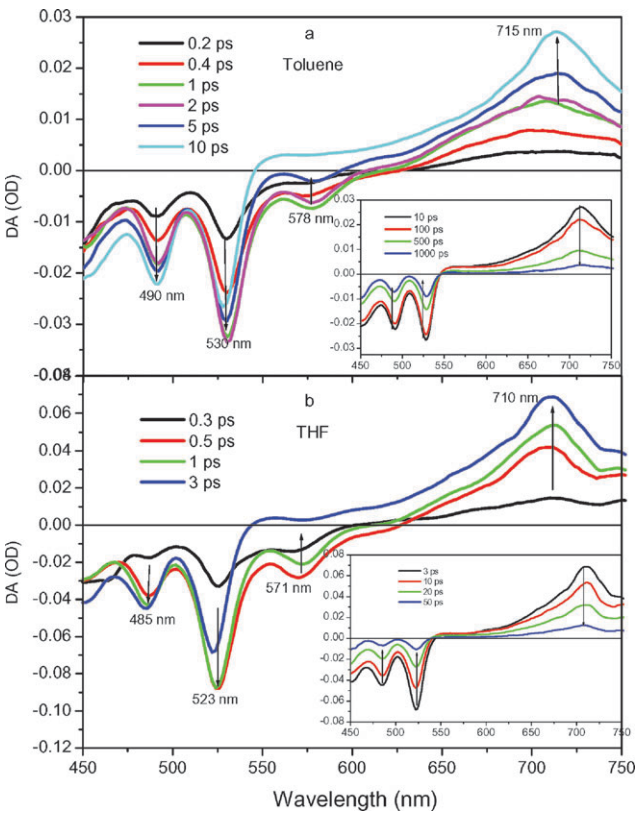

Fig. 4 TA spectra of **1** in toluene (a) and THF (b) within the first 10 ps (3 ps for THF) after 403 nm light excitation. The insets of (a) and (b) show the TA spectra at longer time delays.

UV-Vis absorption spectra of films

Fig. 6(a) displays the spectrum of **1** spin-coated into a thin film, along with those of **1** in toluene, and of a film spin-coated from a 1 : 1 mixture of **OTH** and **PDI** moieties without the covalent linkage. The **1**, **PDI** and **OTH** thin film spectra are red-shifted with respect to their solution counterparts. The red shift is greater in the **PDI** film compared to **1**. Although the peaks are broadened, the vibronic structure is still visible in these spectra. Fig. 6(b) compares the film spectra of **1** and a non-covalently bound 1 : 1 **OTH**–**PDI** mixture, along with a spectrum reconstructed from the sum of the respective absorption spectra of **OTH** and **PDI** films with 1 : 1 ratio. The (0,0) and (0,1) vibronic bands of **PDI** moiety in the spectrum of **1** in toluene at 491 and 527 nm were red-shifted to 499 and 537 nm, respectively in the **1** film. Similar red-shifts have been reported previously and can be explained by the Davydov splitting due to dipole–dipole interactions among adjacent molecules in an amorphous film.[38] The exciton energy displacement $\Delta E = |\mu|^2(1 - 3\cos^2\theta)/r^3$, where r is the distance between the two transition dipoles μ, and θ is the angle between the two dipoles.[39] A much smaller ΔE of 1418 cm^{-1} in the **1** film was observed compared to that of 2135 cm^{-1} in the **PDI** film [calculated from the (0,0) and (0,1) peaks at 493 and 551 nm, respectively]. Smaller energy splitting indicates weaker intermolecular interactions in the **1** film, which is most likely due to larger r and θ values from higher disorder compared to the neat **PDI** film. The enhancement of the (0,1) vibronic band intensity with respect to the (0,0) vibronic intensity in the film spectra suggests the formation of molecular aggregates in these systems.[21,33,40–46] Therefore, the intermolecular coupling between PDI blocks in **1** is weaker due to a lower degree of aggregation than in the reference films.

Comparing with the UV-spectrum of **1** in toluene, the maximum peak position of **1** film shifted from (0,0) to (0,1). The intensity ratio of (0,0) at 527 nm and (0,1) at 491 nm was decreased from 1.6 in toluene to 0.58 on film, indicating well-organized aggregates. A blue shift of the absorption maximum is typical for the formation of face-to-face H-type aggregates, as suggested in perylene bisimide based molecules.[33,44] The peak ratio of the film composed of a

Table 2 Time constants for the charge separation and charge recombination of D–A molecules in toluene and THF excited at different pump wavelengths. The probe wavelength was 710 nm. A_f is the amplitude of a fast CS component that is shorter than the 180 fs instrument response function of the TA system

Molecule	$A_{f,CS}$ (%)	$A_{1,CS}$ (%), $\tau_{1,CS}$/ps	$A_{1,CR}$ (%), $\tau_{1,CR}$/ps	$A_{2,CR}$ (%), $\tau_{2,CR}$/ps	$\tau_{av,CR}$/ps
Toluene, 403 nm pump					
1		100, 1.6	100, 457		
2		100, 1.7	100, 356		
3		100, 1.5	100, 345		
4		100, 0.96	100, 387		
Toluene, 527 nm pump					
1	24	76, 1.4	14, 98	86, 486	432
2	17	83, 0.71	15, 81	85, 403	355
3	17	83, 1.2	25, 130	75, 387	323
4	24	76, 1.2	18, 100	82, 403	348
THF, 403 nm pump					
1	39	61, 2.0	73, 14	27, 63	27.2
2	33	67, 1.6	71, 9.3	29, 44	19.4
3	36	64, 1.9	74, 10.5	26, 53	21.5
4	33	67, 2.0	71, 10.1	29, 47	20.8
THF, 522 nm pump					
1	56	44, 2.2	76, 14	24, 66	26.5
2	54	46, 2.2	79, 9.4	21, 50	17.9
3	53	47, 2.0	80, 12	20, 67	23
4	53	47, 1.6	79, 13	21, 67	24.3

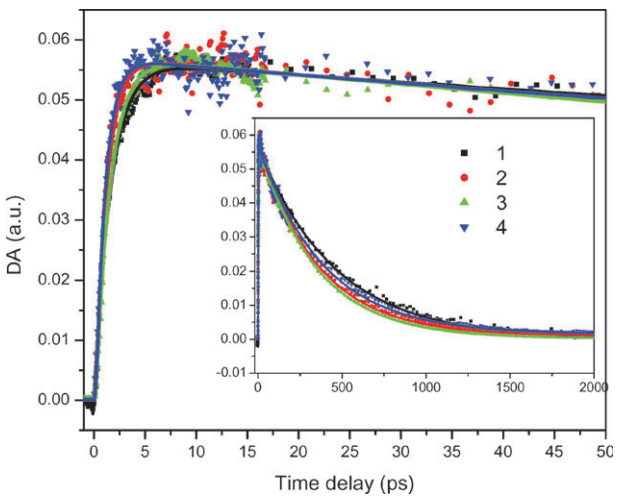

Fig. 5 CS and CR dynamics of **1–4** in toluene probed at the **PDI**$^-$ absorption at 715 nm (excitation at 403 nm). The inset expands the time scale to 2 ns.

1 : 1 mixture of **OTH** and **PDI** (~0.8) is higher than that calculated and for **1** in film. This suggests covalently linked molecules exhibit a higher degree of aggregation than that of non-covalently linked molecular film.

Photoinduced CS and CR kinetics of films

According to UV-Vis spectra, the linear diblock compounds form a high degree of aggregates after spin-coating. At this condition, exciton annihilation and multiphoton processes may easily occur under higher pump power. To find the pump power limit with negligible exciton–exciton annihilation, we compared the electron transfer kinetics at four different pump powers at 50, 100, 300 and 500 nJ. Within error, the traces

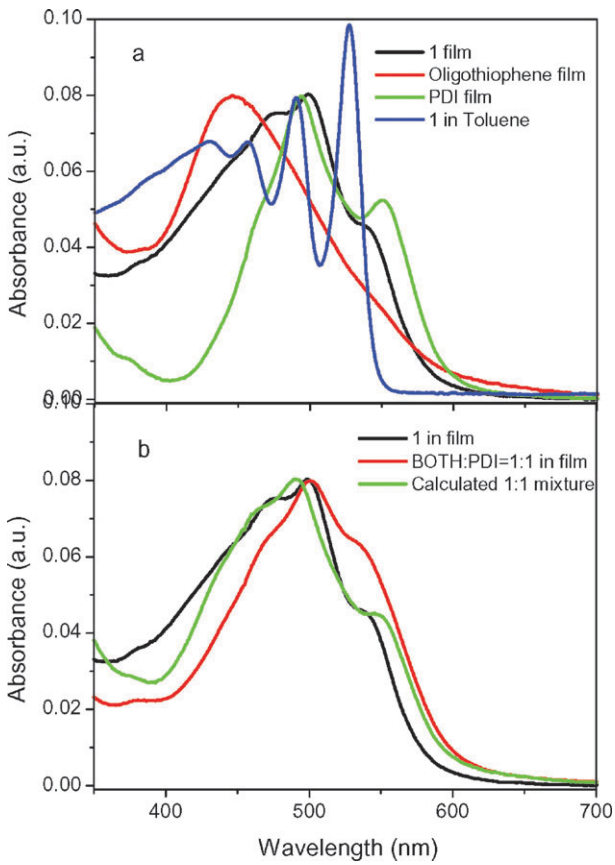

Fig. 6 UV-Vis spectra of films at 298 K (a) **1** in film (black), **OTH** film (red), **PDI** film (green), and **1** in toluene (blue). (b) Calculated spectra from the **OTH** and **PDI** film spectra with 1 : 1 **OTH** : **PDI** ratio (green), measured spectra of **1** film (black) and the 1 : 1 mixture of **OTH** and **PDI** film (red). The films were spin-coated at room temperature without annealing.

from 50 and 100 nJ pump power are identical but the CR rates of 300 and 500 nJ increase with increasing pump power. This indicates that at the pump power below 100 nJ, the exciton annihilation and multiphoton processes appears to be negligible. The subsequent measurements were thus carried out at exciton power level of 100 nJ to have better signal.

Fig. 7(a) shows the TA spectra of **PDI** and **4** films at 0.5 ps excited at 530 nm. The former has a broad absorption band from 590 to 760 nm due to ^{1}**PDI*** similar to the solution samples,[31] whereas the latter has a distinctive, narrower peak centered at 730 nm due to the **PDI**$^{-}$ absorption, which has been characterized in chemically reduced PDI films.[36] Hence, it is indicative of the generation of **PDI**$^{-}$ due to the PET in $<$0.5 ps after the excitation and consistent with the observed CS kinetics results (Table 3). Compared with the TA spectra of **PDI**$^{-}$ in solution (Fig. 4), the distinctive **PDI**$^{-}$ absorption feature in films is red-shifted by 15–20 nm due to strongly interacting π–π stacked PDI molecules.[36] Hereafter, we report all the CS and CR dynamics for those dyads on films by monitoring the evolution of **PDI**$^{-}$ peak at 725–735 nm. Meanwhile, the steady-state fluorescence spectra of the films

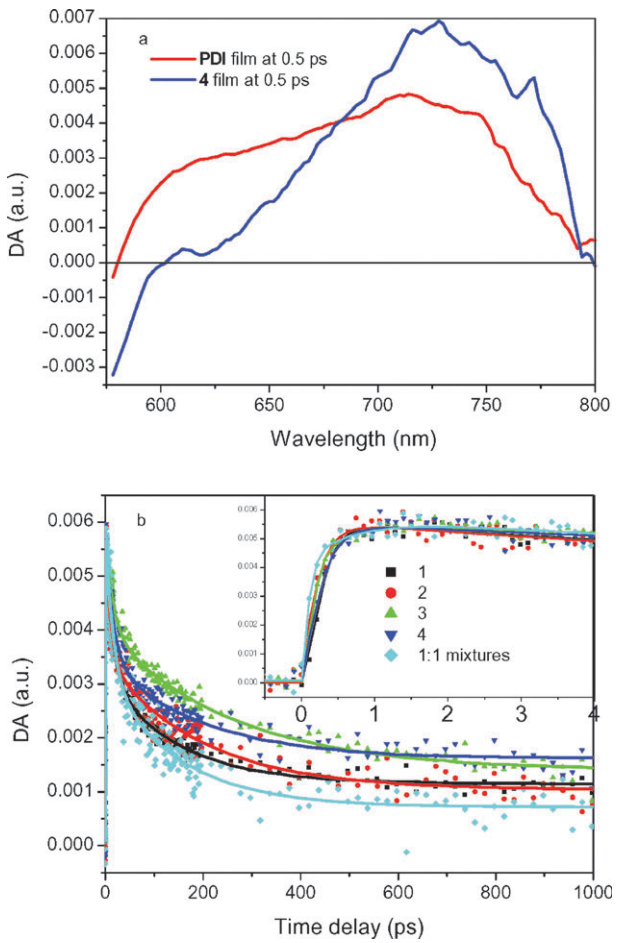

Fig. 7 (a) Comparison of TA spectra of the **PDI** and **4** films at 0.5 ps with the excitation at 530 nm; (b) kinetic traces of **1–4** and 1 : 1 **OTH–PDI** in pristine films probed at 725 nm with 403 nm excitation. These traces have been normalized at ~1 ps for comparison. The inset is an expanded view of the data at early delay times.

indicated that >95% of their fluorescence is quenched compared to neat OTH film as expected because the quenching is due to the photoinduced intramolecular CS.

Fig. 7(b) compares the CS and CR kinetics in films of **1–4** and a non-covalently linked 1 : 1 **OTH–PDI** composite probed at the **PDI**$^{-}$ absorption of 725 nm after 403 nm excitation. The CS time constants are similar but the CR time constants vary and decrease in the order of **3** > **4** ≈ **2** > **1** > 1 : 1 **OTH–PDI**, which is distinctively different from the solution results, where their time constants are virtually indistinguishable (Fig. 5 and Table 2).

The drastically different dynamic behavior of these dyads in solutions as isolated molecules and in films as aggregates prompted us to investigate their correlation with molecular packing structures in films of **1–4** by GISAXS and GIWAXS. The pristine **1** film shows no diffraction peaks due to its complete disorder in molecular packing (Fig. 10). In contrast, the pristine **3** film has three in-plane diffraction peaks at q = 0.26, 0.48 and 0.81 Å^{-1}, as well as one out-of-plane peak at q = 0.82 Å^{-1}. The in-plane peaks are assigned to (100), (200) and (300) diffractions of a lamellae structure. It is interesting to note that a broad peak extended from q = 1.2 Å^{-1} to our detection limit at q = 1.4 Å^{-1} (the inset of Fig. 10(b)) on both pristine films. Although we do not have a large enough q range to clearly show the whole peak, the trend suggests possible π–π stacking in both films. Further GIXS experiments in the q > 1.4 Å^{-1} range are in progress for determination of the precise d-spacing of the π–π stacking in films. When comparing the kinetics of the pristine and annealed films with the structural information stated above, the CR kinetics in films are well correlated with the molecular packing order in the films revealed by the GIXS results. Despite of their similar CS rates, the more ordered **3** film shows a slower CR rate than the disordered **1** film, suggesting that the ordered packing enhances the charge carrier mobility to assist electron and hole diffusion (Fig. 7(b)). The correlation between the CR rate and the packing indicates the importance of correct nanomorphology for the OPV device performance. Direct measurements of charge carrier concentration at a longer time after the excitation will be investigated in the future.

Effect of annealing on the CS and CR kinetics of films

Enhanced photovoltaic efficiencies in polymer/PCBM solar cells[47–51] were observed after annealing and were attributed to an increased charge mobility due to both improved crystallinity in films and a better mixing of the polymers and PCBM.[12,52,53] In our study, the CS rate of **1** was not affected by annealing while its CR rate was slowed down by annealing (120 °C for 60 min) (Fig. 8).

Meanwhile, the effect of annealing on molecular packing structures was shown by the GIXS patterns of the pristine and annealed films of **1** (Fig. 9). The in-plane and out-of-plane GIXS profiles are shown in Fig. 10. Although no diffraction pattern was observed on the pristine film, a sharp in-plane peak at q = 0.122 Å^{-1}, and a small peak at 0.24 Å^{-1} appeared after annealing at 125 °C. Simultaneously, out-of-plane peaks appeared at 0.14, 0.28 and 0.41 Å^{-1}, respectively. This

Table 3 Time constants for the charge separation and charge recombination of D–A array films[a]

Films	$A_{1,CS}$ (%), $\tau_{1,CS}$/ps	$A_{1,CR}$ (%), $\tau_{1,CR}$/ps	$A_{2,CR}$ (%), $\tau_{2,CR}$/ps	$\tau_{av,CR}$/ps
1	100, 0.19	54, 14.4	46, 146	75
2	100, 0.19	47, 11.1	53, 197	110
3	100, 0.35	37, 17.7	63, 261	171
4	100, 0.24	53, 16.9	47, 196	101
1 : 1 **OTH–PDI** mixture	100, 0.40	50, 14.4	50, 109	62
1 annealed	100, 0.35	43, 10.6	57, 172	103

[a] Measured at room temperature with 403 nm excitation.

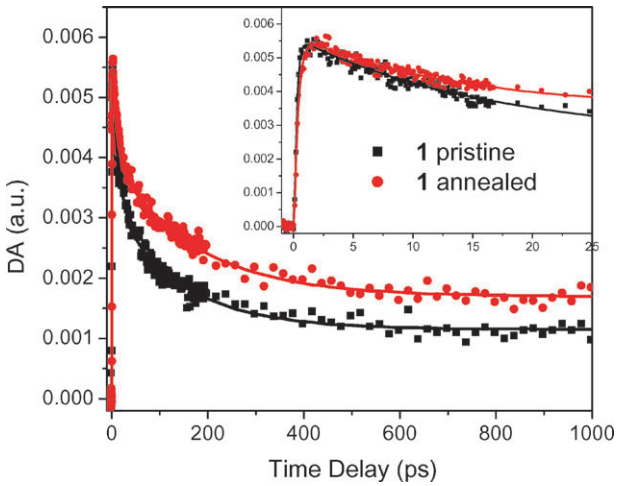

Fig. 8 Comparison of dynamics of **1** in its pristine and annealed film. Inset is an expanded view of early delay times.

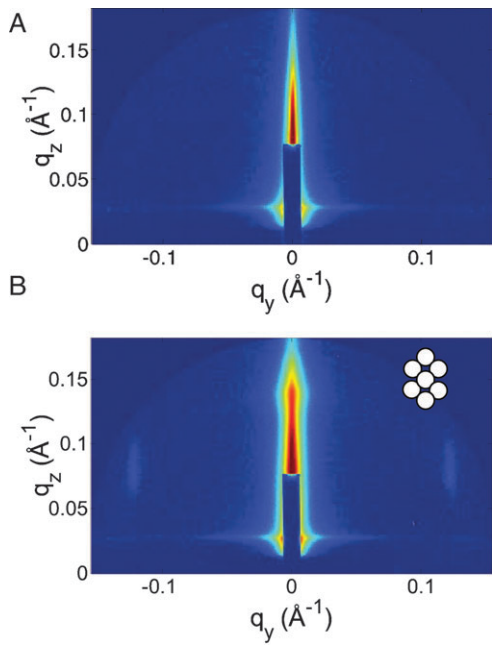

Fig. 9 GISAXS pattern measured at incident angle $\alpha_I = 0.2^\circ$ of molecule **1** before (a) and after (b) annealing. The inset of panel b shows the illustration of hexagonal structure. The q_y and q_z axes correspond to the parallel and perpendicular scattering vectors, respectively. The presence of the two elongated peaks, as well as the enhanced peak at q_z, shows the formation of hexagonal packing in the annealed film. These peaks are roughly 60° with respect to the q_z plane. Please see the text for more details on these peaks.

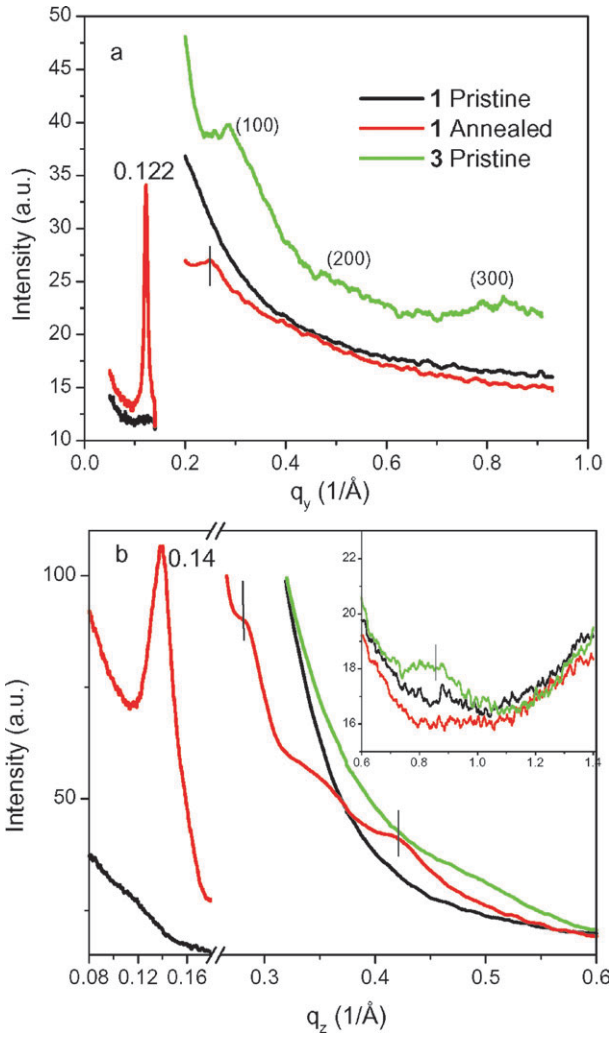

Fig. 10 (a) In-plane and (b) out-of-plane GISAXS and GIWAXS profiles of pristine **1** film, annealed **1** film, and pristine **3** film. The inset of panel b depicts a larger q range. The X-ray energy was 7.35 keV.

diffraction pattern suggests a hexagonal packing structure with a d-spacing of ~5.2 nm, a dimension close to the full length of **1**.[54] A schematic of the hexagonal packing structure is shown in the inset of Fig. 9(b), which demonstrates the increased crystallinity in **1** film after the thermal annealing. Consequently, this more ordered structure will facilitate photogenerated charge carrier diffusion away from the charge separation site, and hence reduce geminate charge recombination, which decreases solar cell efficiency.

Discussion

Effect of solvent polarity on the PET dynamics

The rate and efficiency of photoinduced charge separation are essential factors in photovoltaic applications and are intimately related to the structural factors of D and A. Several structural parameters, such as relative distances and orientations between D and A, will affect the rate constant of electron-transfer k_{ET}. Because the initial intramolecular charge separation can be considered a non-adiabatic electron transfer reaction, its rate constant k_{ET} can be described by the Marcus equation for the electron transfer:[55]

$$k_{ET} = \frac{2\pi}{\hbar} H_{DA}^2 (4\pi\lambda k_B T)^{-1/2} \exp\left[-\frac{(\Delta G + \lambda)^2}{4\lambda k_B T}\right] \quad (1)$$

where H_{DA} is the electronic coupling matrix between D and A, ΔG is the free energy of the reaction, and the total reorganization energy λ is the sum of the intramolecular reorganization energy (λ_i) and the solvent reorganization energy (λ_s). The solvent-independent inner term λ_i arises from the energy changes accompanying alteration in bond lengths and bond angles during the ET process.[31] The internal organization energy was assumed to be λ_i = 0.3 eV according to the value reported on several thiophene–C_{60} and oligo(*p*-phenylenevinylene)–perylene diimide donor–acceptor systems.[20,22,27,56] This value may be the upper limit of the actual internal reorganization energy due to the delocalization of the **OTH**$^+$ cation on the longer thiophene chain.

The solvent term λ_s arises from energy differences due to the solvent molecule reorientation around the reactant (*i.e.* D*–A or D–A* in the CS reaction) and the product (*i.e.* D^+–A^- in the CS reaction). If the surrounding solvent is treated as a dielectric continuum, λ_s can be expressed by:[57]

$$\lambda_s = \frac{(\Delta e)^2}{4\pi\varepsilon_0}\left[\frac{1}{2a_D} + \frac{1}{2a_A} - \frac{1}{r_{DA}}\right]\left[\frac{1}{\varepsilon_{op}} - \frac{1}{\varepsilon_s}\right] \quad (2)$$

where Δe is the charge transferred in the ET process; a_D and a_A are the radii of D and A, respectively; r_{DA} is the center-to-center distance between D and A; ε_0 is the permittivity of vacuum; and ε_{op} and ε_s are the optical and static dielectric constants, respectively. The values for toluene are ε_{op} = 2.23 and ε_s = 2.38 while the values for THF are ε_{op} = 1.98 and ε_s = 7.51. The radius of **PDI**$^-$ anion, r^-, was set to 4.7 Å, as reported previously. If the side chain is excluded, the radius of **OTH**$^+$ cation can be calculated *via* the van der Waals volume through $r^+ = (3 \times 10^{24} M/4\pi\rho N_A)^{1/3}$.[22] The density of the oligothiophene without a side chain (ρ = 1.51 g cm^{-3}) is known to be independent of the length. This approach results in r^+ = 5.6 Å. The value of r_{DA} = 15.3 Å is therefore obtained by assuming localized charges at the center of **OTH** and **PDI** with a benzene link between them. These values for the radii result in λ_s values of 0.047 and 0.73 eV for toluene and THF, respectively. Therefore, the total reorganization energy λ is 0.347 eV for toluene and 1.03 eV for THF.

Table 4 shows the Gibbs free energy and reorganization values for all molecules studied in these experiments. The Gibbs energy values were obtained using assumptions and equations derived previously.[28,53] These values show that the CR driving force for all molecules was higher in toluene, which correlates well with the slower recombination times. With these values, it is shown that the activation barriers of CS in both toluene and THF are small because the differences between $-\Delta G_{CS}$ and λ are small. In such a condition, the CS rate is controlled by the electronic coupling term, H_{DA}, (see eqn (1)) and the polarity of the solvent plays a less important role. The electronic coupling is directly affected by the overlap of D and A wavefunctions, which depends on the nature of the spacer and the separation of D and A. Because D and A in **1–4** are only separated by a single rigid benzene bridge, rather strong electronic coupling between them is expected. Consequently, the CS rates for these molecules are similar in toluene and THF. In contrast, the charge recombination lies in the "inverted" region ($-\Delta G > \lambda$). The CR rate is expected to decrease with increasing driving force ΔG_{CR}. Therefore, the slower recombination rates for **1–4** in toluene compared to THF can be explained by the higher ΔG_{CR} values for the toluene solutions.

Photoinduced CS and CR in films

The structure–efficiency correlation in conjugated polymer-based devices has been recognized in recent years.[51,58,59] The field–effect mobility of poly(3-hexylthiophene) (**P3HT**) varies by several orders of magnitude with the film morphology controlled through side chains,[58,59] solvents,[49,52] annealing temperatures,[47,48,50] and molecular weights.[60–64] For example, Tu *et al.*[59] found that the solar cell power conversion efficiency decreased by a factor of 25 and the hole mobility dropped almost four orders of magnitude when **P3HT** with 8% 3.3′-bithiophene branches was used. The AFM results show a neat lamellar structure for non-branched **P3HT**/**PCBM** film, whereas the branched **P3HT** results in the formation of larger, irregular aggregates. Babel and Jenekhe[58] found that the hexyl side chain had the best hole mobility (1×10^{-2} cm^2 V^{-1} s^{-1}) while a drop of three orders of magnitude in the hole mobility was observed for poly(3-dodecylthiophene). These results revealed the importance of the molecular packing morphology on the carrier mobility.

However, before we can ensure sufficiently high charge carrier mobility in organic films for OPV applications, we must make sure that the CR rates are sufficiently long for separated charges to diffuse away from where they are separated. At this stage of the study, we investigate the effect of the varying the end group of the PDI moiety on the molecular packing in **1–4** (Fig. 1) and its influence on the photoinduced CS and CR dynamics. Although the CS and CR rates for **1–4** are similar in solution, their corresponding CR rates in pristine films deviate from each other, while their CS rates remain similar. The average rate constant of the CR processes for the pristine **3** film is 171 ps, which is 2.3 times that of **1** film (75 ps). The CR rates of covalently linked D–A dyads in films are slower than that of the non-covalently linked D/A mixture film. The difference indicates that the packing of the **OTH** donor and the **PDI** acceptor in the latter film is relatively random. On one hand, it may undergo phase separation, forming domains larger than the exciton diffusion

Table 4 Gibbs free energy and reorganization values for **1–4**

Molecules	Solvent	ΔG_{CS}/eV	ΔG_{CR}/eV	λ/eV	$\Delta G^{\ddagger}_{CS}$/eV	$\Delta G^{\ddagger}_{CR}$/eV
1	Toluene	−0.57	−1.76	0.347	3.6×10^{-2}	1.44
	THF	−1.09	−1.36	1.03	8.7×10^{-4}	2.6×10^{-2}
2	Toluene	−0.61	−1.72	0.347	5.0×10^{-2}	1.36
	THF	−1.13	−1.32	1.03	2.4×10^{-3}	2.0×10^{-2}
3	Toluene	−0.60	−1.70	0.347	4.6×10^{-2}	1.32
	THF	−1.12	−1.33	1.03	2.4×10^{-3}	2.2×10^{-2}
4	Toluene	−0.62	−1.71	0.347	5.4×10^{-2}	1.34
	THF	−1.14	−1.19	1.03	2.9×10^{-3}	6.2×10^{-3}

length and slowing down the CS process. On the other hand, it may form directly stacked D and A, promoting geminate recombination. The similar CS rates and different CR rates between the covalently linked and non-covalently linked D–A in pristine films indicate that the latter scenario is more likely. The accidental face-to-face D/A packing in the non-covalently linked D/A film permits the observed CS rates, while the geminate recombination of the charges is so fast that it overwhelms the charge carrier diffusion, resulting in the fast CR rate. In contrast, the covalently linked D and A arrays decrease the accidental intermolecular face-to-face D/A packing with structural constraints due to their larger sizes than individual D or A blocks. Consequently, the CR rate due to geminate recombination is reduced in the films from covalently linked dyads. The lesson learned from our studies is that the covalent linking D–A is a good strategy in preventing geminate recombination in films. However, a better intramolecular phase separation between D and A blocks needs to be implemented in the future to promote simultaneous intermolecular D–D and A–A stacking into continuous channels for electron and hole diffusion after they are separated in films. Future studies in this direction are in progress.

Because **2**, **3** and **4** have conjugated side groups, and **1** has a long alkyl chain, (Fig. 1), **2**, **3** and **4** have less steric hindrance than **1** when they assemble in films. According to the GIXS results, **3** and **2** (not shown) exhibit a lamellae structure and have a higher degree of packing than **1** in films. As a result, much slower CR rates for pristine films of **2**, **3** and **4** than those of **1** were observed due to the improved charge mobility along the direction of packing to allow the charges to diffuse further.

A comparison of the CR rates before and after annealing of the films also suggests the importance of stacking in extending the lifetimes of charge separated species. Although the annealing slows down the CR rates in all **1–4** films, its effect is most significant for **1** film. This observation suggests the following: (1) the bulky alkyl end group in **1** prohibits packing in pristine films due to the steric hindrance exerted by such a large group compared to other end groups in **2–4**, and (2) the annealing enables the large but flexible branched alkyl groups to alter their configurations for an improved packing while it has only small influence on the rigid end groups in **2–4**.

The enhancement of charge separation state lifetimes is the first step for generating abundant charge carriers in photovoltaic devices. A longer-lived charge-separated species is a prerequisite for charge carriers to diffuse away from where they form and thus reduce wasteful charge recombination. We have shown in this study that the efficiency of OPV can be improved by attaching side groups, and by annealing, as well as by forming bi-continuous channels with isolated donor–acceptor blocks. Our current and future studies will combine charge carrier kinetics measurements with structural studies to investigate the structure/performance of these self-assembled potential OPV materials consisting of D and A blocks systematically.

Summary

Initial photoinduced CS and CR dynamics of four linear D–A dyads with a benzene linker and different end groups were characterized using ultrafast transient spectroscopy in solutions and films. All molecules have much faster CS rates than CR rates in both polar THF and much less polar toluene. The differences in rates are elucidated by the differences in the reorganization energy λ from the Marcus equation. Annealing the films most significantly improves the packing for molecules with bulky alkyl end groups, which results in a slower CR rate. On molecules with smaller end groups, it has limited effect. The results imply that better packing facilitates the charge transport and reduces geminate recombination, which is a process than can reduce solar cell efficiency. We have shown that covalently linking D and A blocks is a good strategy for implementing structural constraints to lower geminate recombination in films by preventing accidental face-to-face D/A packing. An improved intramolecular phase separation between D and A blocks will be needed in future studies to facilitate a better π–π stacking among D blocks and among A blocks, respectively, for better charge carrier transport in films, which is ultimately linked to the device performance. Although the slow charge carrier transport dynamics will determine the final performance of the films in an OPV device, the initial CS and CR dynamics and their correlation with molecular packing described will provide information on rational design of the materials. A complete characterization from initial CS to charge carrier transport in film is needed and has been planned in future studies.

Acknowledgements

We would like to acknowledge the supports by UC/ANL collaborative seed grant (L. Y. and L. X. C.), Northwestern University setup fund, and the Division of Chemical Sciences, Office of Basic Energy Sciences, the U. S. Department of Energy under contract W-31-109-Eng-38 (for L. X. C.). The facilities of the Advanced Photon Source are supported by Office of Basic Energy Sciences, the U. S. Department of Energy under contract W-31-109-Eng-38.

References

1 C. J. Brabec, V. Dyakonov, J. Parisi and N. S. Sariciftci, *Organic Photovoltaics: Concepts and Realization*, Springer, New York, 2003.
2 K. M. Coakley and M. D. McGehee, *Chem. Mater.*, 2004, **16**, 4533–4542.
3 G. Li, V. Shrotriya, Y. Yao, J. Huang and Y. Yang, *J. Mater. Chem.*, 2007, **17**, 3126–3140.
4 S. Gunes, H. Neugebauer and S. Sariciftci Niyazi, *Chem. Rev.*, 2007, **107**, 1324–1338.
5 J. Peet, J. Y. Kim, N. E. Coates, W. L. Ma, D. Moses, A. J. Heeger and G. C. Bazan, *Nat. Mater.*, 2007, **6**, 497–500.
6 J. J. M. Halls, C. A. Walsh, N. C. Greenham, E. A. Marseglia, R. H. Friend, S. C. Moratti and A. B. Holmes, *Nature*, 1995, **376**, 498–500.
7 J. Liu, T. Tanaka, K. Sivula, A. P. Alivisatos and J. M. J. Frechet, *J. Am. Chem. Soc.*, 2004, **126**, 6550–6551.
8 W. U. Huynh, J. J. Dittmer and A. P. Alivisatos, *Science (Washington, DC)*, 2002, **295**, 2425–2427.
9 W. U. Huynh, X. Peng and A. P. Alivisatos, *Adv. Mater.*, 1999, **11**, 923–927.
10 G. Li, V. Shrotriya, J. Huang, Y. Yao, T. Moriarty, K. Emery and Y. Yang, *Nat. Mater.*, 2005, **4**, 864–868.
11 M. Reyes-Reyes, K. Kim and D. L. Carroll, *Appl. Phys. Lett.*, 2005, **87**, 083506/083501–083506/083503.
12 X. Yang, J. K. J. Van Duren, R. A. J. Janssen, M. A. J. Michels and J. Loos, *Macromolecules*, 2004, **37**, 2151–2158.
13 E. H. A. Beckers, Z. Chen, S. C. J. Meskers, P. Jonkheijm, A. P. H. J. Schenning, X.-Q. Li, P. Osswald, F. Wuerthner and R. A. J. Janssen, *J. Phys. Chem. B*, 2006, **110**, 16967–16978.
14 E. Frankevich, H. Ishii, Y. Hamanaka, T. Yokoyama, A. Fuji, S. Li, K. Yoshino, A. Nakamura and K. Seki, *Phys. Rev. B: Condens. Matter Mater. Phys.*, 2000, **62**, 2505–2515.
15 D. E. Markov, E. Amsterdam, P. W. M. Blom, A. B. Sieval and J. C. Hummelen, *J. Phys. Chem. A*, 2005, **109**, 5266–5274.
16 P. Peumans, S. Uchida and S. R. Forrest, *Nature*, 2003, **425**, 158–162.
17 J. G. Muller, J. M. Lupton, J. Feldmann, U. Lemmer, M. C. Scharber, N. S. Sariciftci, C. J. Brabec and U. Scherf, *Phys. Rev. B: Condens. Matter Mater. Phys.*, 2005, **72**, 195208/195201–195208/195210.
18 J. G. Muller, U. Lemmer, J. Feldmann and U. Scherf, *Phys. Rev. Lett.*, 2002, **88**, 147401/147401–147401/147404.
19 M. J. Ahrens, L. E. Sinks, B. Rybtchinski, W. Liu, B. A. Jones, J. M. Giaimo, A. V. Gusev, A. J. Goshe, D. M. Tiede and M. R. Wasielewski, *J. Am. Chem. Soc.*, 2004, **126**, 8284–8294.
20 E. H. A. Beckers, P. A. Van Hal, A. Dhanabalan, S. C. J. Meskers, J. Knol, J. C. Hummelen and R. A. J. Janssen, *J. Phys. Chem. A*, 2003, **107**, 6218–6224.
21 R. Gomez, D. Veldman, R. Blanco, C. Seoane, J. L. Segura and R. A. J. Janssen, *Macromolecules*, 2007, **40**, 2760–2772.
22 E. Peeters, P. A. van Hal, J. Knol, C. J. Brabec, N. S. Sariciftci, J. C. Hummelen and R. A. J. Janssen, *J. Phys. Chem. B*, 2000, **104**, 10174–10190.
23 E. Peeters, P. A. Van Hal, S. C. J. Meskers, R. A. J. Janssen and E. W. Meijer, *Chem.–Eur. J.*, 2002, **8**, 4470–4474.
24 A. M. Ramos, E. H. A. Beckers, T. Offermans, S. C. J. Meskers and R. A. J. Janssen, *J. Phys. Chem. A*, 2004, **108**, 8201–8211.
25 B. Rybtchinski, L. E. Sinks and M. R. Wasielewski, *J. Am. Chem. Soc.*, 2004, **126**, 12268–12269.
26 B. Rybtchinski, L. E. Sinks and M. R. Wasielewski, *J. Phys. Chem. A*, 2004, **108**, 7497–7505.
27 P. A. Van Hal, J. Knol, B. M. W. Langeveld-Voss, S. C. J. Meskers, J. C. Hummelen and R. A. J. Janssen, *J. Phys. Chem. A*, 2000, **104**, 5974–5988.
28 E. Fron, T. D. M. Bell, A. Van Vooren, G. Schweitzer, J. Cornil, D. Beljonne, P. Toele, J. Jacob, K. Muellen, J. Hofkens, M. Van der Auweraer and F. C. De Schryver, *J. Am. Chem. Soc.*, 2007, **129**, 610–619.
29 E. Fron, R. Pilot, G. Schweitzer, J. Qu, A. Herrmann, K. Muellen, J. Hofkens, M. Van der Auweraer and F. C. De Schryver, *Photochem. Photobiol. Sci.*, 2008, **7**, 597–604.
30 E. Fron, G. Schweitzer, J. Jacob, A. Van Vooren, D. Beljonne, K. Mullen, J. Hofkens, M. Van der Auweraer and F. C. De Schryver, *ChemPhysChem*, 2007, **8**, 1386–1393.
31 L. X. Chen, S. Xiao and L. Yu, *J. Phys. Chem. B*, 2006, **110**, 11730–11738.
32 L. X. Chen, D. Polshakov, S. Q. Xiao, Y. Liang and L. Yu, 2008, unpublished results.
33 A. D. Q. Li, W. Wang and L.-Q. Wang, *Chem.–Eur. J.*, 2003, **9**, 4594–4601.
34 R. H. Goldsmith, O. DeLeon, T. M. Wilson, D. Finkelstein-Shapiro, M. A. Ratner and M. R. Wasielewski, *J. Phys. Chem. A*, 2008, **112**, 4410–4414.
35 R. H. Goldsmith, L. E. Sinks, R. F. Kelley, L. J. Betzen, W. Liu, E. A. Weiss, M. A. Ratner and M. R. Wasielewski, *Proc. Natl. Acad. Sci. USA*, 2005, **102**, 3540–3545.
36 R. O. Marcon and S. Brochsztain, *Langmuir*, 2007, **23**, 11972–11976.
37 D. Gosztola, M. P. Niemczyk, W. Svec, A. S. Lukas and M. R. Wasielewski, *J. Phys. Chem. A*, 2000, **104**, 6545–6551.
38 J. Mizuguchi, *J. Appl.Phys.*, 1998, **84**, 4479–4486.
39 M. Kasha, H. R. Rawls and M. A. El-Bayoumi, *Pure Appl. Chem.*, 1965, **11**, 371–392.
40 X. Li, L. E. Sinks, B. Rybtchinski and M. R. Wasielewski, *J. Am. Chem. Soc.*, 2004, **126**, 10810–10811.
41 J. M. Giaimo, J. V. Lockard, L. E. Sinks, A. M. Scott, T. M. Wilson and M. R. Wasielewski, *J. Phys. Chem. A*, 2008, **112**, 2322–2330.
42 T. van der Boom, R. T. Hayes, Y. Zhao, P. J. Bushard, E. A. Weiss and M. R. Wasielewski, *J. Am. Chem. Soc.*, 2002, **124**, 9582–9590.
43 J. M. Giaimo, A. V. Gusev and M. R. Wasielewski, *J. Am. Chem. Soc.*, 2002, **124**, 8530–8531.
44 W. Wang, L.-S. Li, G. Helms, H.-H. Zhou and A. D. Q. Li, *J. Am. Chem. Soc.*, 2003, **125**, 1120–1121.
45 A. E. Clark, C. Qin and A. D. Q. Li, *J. Am. Chem. Soc.*, 2007, **129**, 7586–7595.
46 J. J. Han, W. Wang and A. D. Q. Li, *J. Am. Chem. Soc.*, 2006, **128**, 672–673.
47 Y. Kim, S. A. Choulis, J. Nelson, D. D. C. Bradley, S. Cook and J. R. Durrant, *J. Mater. Sci.*, 2005, **40**, 1371–1376.
48 Y. Kim, S. A. Choulis, J. Nelson, D. D. C. Bradley, S. Cook and J. R. Durrant, *Appl. Phys. Lett.*, 2005, **86**, 063502/063501–063502/063503.
49 T.-F. Guo, T.-C. Wen, G. L. v. Pakhomov, X.-G. Chin, S.-H. Liou, P.-H. Yeh and C.-H. Yang, *Thin Solid Films*, 2008, **516**, 3138–3142.
50 K. Inoue, R. Ulbricht, P. C. Madakasira, W. M. Sampson, S. Lee, J. Gutierrez, J. Ferraris and A. A. Zakhidov, *Synth. Met.*, 2005, **154**, 41–44.
51 T. Erb, U. Zhokhavets, G. Gobsch, S. Raleva, B. Stuehn, P. Schilinsky, C. Waldauf and C. J. Brabec, *Adv. Funct. Mater.*, 2005, **15**, 1193–1196.
52 S. Miller, G. Fanchini, Y.-Y. Lin, C. Li, C.-W. Chen, W.-F. Su and M. Chhowalla, *J. Mater. Chem.*, 2008, **18**, 306–312.
53 X. Yang, J. Loos, S. C. Veenstra, W. J. H. Verhees, M. M. Wienk, J. M. Kroon, M. A. J. Michels and R. A. J. Janssen, *Nano Lett.*, 2005, **5**, 579–583.
54 B. Lee, I. Park, J. Yoon, S. Park, J. Kim, K.-W. Kim, T. Chang and M. Ree, *Macromolecules*, 2005, **38**, 4311–4323.
55 R. A. Marcus, *J. Chem. Phys.*, 1965, **43**, 3477–3489.
56 E. H. A. Beckers, S. C. J. Meskers, A. P. H. J. Schenning, Z. Chen, F. Wuerthner, P. Marsal, D. Beljonne, J. Cornil and R. A. J. Janssen, *J. Am. Chem. Soc.*, 2006, **128**, 649–657.
57 H. Oevering, M. N. Paddon-Row, M. Heppener, A. M. Oliver, E. Cotsaris, J. W. Verhoeven and N. S. Hush, *J. Am. Chem. Soc.*, 1987, **109**, 3258–3269.
58 A. Babel and S. A. Jenekhe, *Synth. Met.*, 2005, **148**, 169–173.
59 G. Tu, A. Bilge, S. Adamczyk, M. Forster, R. Heiderhoff, L. J. Balk, D. Muehlbacher, M. Morana, M. Koppe, M. C. Scharber, S. A. Choulis, C. J. Brabec and U. Scherf, *Macromol. Rapid Commun.*, 2007, **28**, 1781–1785.
60 C. Goh, R. J. Kline, M. D. McGehee, E. N. Kadnikova and J. M. J. Frechet, *Appl. Phys. Lett.*, 2005, **86**, 122110/122111–122110/122113.

61 R. J. Kline, M. D. McGehee, E. N. Kadnikova, J. Liu, J. M. J. Frechet and M. F. Toney, *Macromolecules*, 2005, **38**, 3312–3319.
62 R. J. Kline, M. D. McGehee, E. N. Kadnikova, J. Liu and J. M. J. Frechet, *Adv. Mater.*, 2003, **15**, 1519–1522.
63 M. Trznadel, A. Pron, M. Zagorska, R. Chrzaszcz and J. Pielichowski, *Macromolecules*, 1998, **31**, 5051–5058.
64 A. Zen, J. Pflaum, S. Hirschmann, W. Zhuang, F. Jaiser, U. Asawapirom, J. P. Rabe, U. Scherf and D. Neher, *Adv. Funct. Mater.*, 2004, **14**, 757–764.